

Magnetic order and energy-scale hierarchy in artificial spin ice

Henry Stopfel,^{1,*} Erik Östman,¹ Ioan-Augustin Chioar,¹ Unnar Arnalds,² David Greving,³ Thomas P. A. Hase,³ Aaron Stein,⁴ Björgvin Hjörvarsson,¹ and Vassilios Kapaklis¹

¹*Department of Physics and Astronomy, Uppsala University, Box 516, SE-75120, Uppsala, Sweden*

²*Science Institute, University of Iceland, Reykjavik, Iceland*

³*Department of Physics, University of Warwick, Coventry, United Kingdom*

⁴*Center for Functional Nanomaterials, Brookhaven National Laboratory, Upton, New York 11973, USA*

(Dated: December 14, 2024)

The interplay of multiple length- and energy-scales is crucial for the understanding of the properties of many physical systems. Artificial ferroic structures can serve as model systems for investigating the outcome of such an interplay. These offer an experimental framework for the definition and tuning of length- and energy-scales by geometry design, while simultaneously facilitating direct access to the system microstates. Here we employ artificial magnetic nano-structures, with varying length-scales of the interacting elements^{1,2} in an attempt to experimentally highlight the importance of distinct energy-scales on the collective magnetic ordering. Utilizing the mesoscopic nature of these architectures and magnetic microscopy techniques, we image the magnetic states in thermal realizations of such systems^{3,4}. In combination with reciprocal space analysis tools, like the magnetic spin structure factor⁵⁻⁷, we reveal the impact of the combination of distinct energy- and length-scales on the magnetic ordering. Our findings provide a conceptual and experimental framework for understanding the role that the energy-scale hierarchy plays in the short-range order of artificial magnetic architectures and beyond.

Initially introduced as a playground for the experimental investigation of magnetic frustration effects⁸, the artificial spin ice framework has evolved into a complex field of research in which collective phenomena can be designed, controlled and directly visualized employing nano-characterization techniques². This has motivated the experimental investigation of celebrated classical spin models^{9,10}, some of which display non-conventional and exotic magnetic phases^{5-7,11}. Furthermore, given the large freedom in design, new topologies that promote non-conventional emergent order can be experimentally manufactured and further investigated, particularly by employing thermally-active versions of these artificial nano-architectures which would facilitate the exploration of the complex energetic manifolds in a super-paramagnetic regime^{3,4,12-15}. A variety of such magnetic systems have been proposed by Morrison et al.¹, with a particular attention given to the so-called Shakti lattice, a variation of the square ice geometry involving the sys-

tematic removal of 25% of the square ice lattice elements and the merging of certain pairs of islands, as depicted in Fig. 1. Theoretical and numerical studies have predicted the development of an emergent order in such a geometry¹⁶, retrieving the features of the 6-vertex model⁹ on a larger length-scale. This behavior has been experimentally evidenced by Gilbert *et al.*¹⁷ for the Shakti lattice (SH), as well as the so-called modified Shakti lattice (mSH), in which the merging of islands is not performed, thus containing uniquely-sized elements, as illustrated in Fig. 1. However, given the mesoscopic nature of the system elements and the fact that they are subject to thermal fluctuations in a super-paramagnetic regime, different activation energies are expected for the long and the short islands of the Shakti lattice, potentially affecting the development of magnetic order. While the vertex populations of the three- and the four-fold coordinated vertices have been experimentally determined for a range of interactions¹⁷, the importance of the two energy-scales and the impact of this difference in the activation energy was not been properly addressed so far.

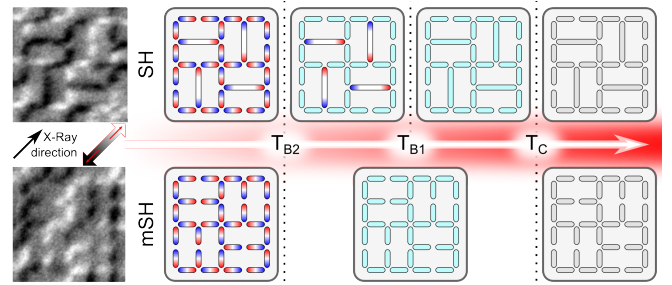


FIG. 1. The Shakti (SH) and modified-Shakti (mSH) lattices. A schematic representation of the SH and the mSH lattices and their magnetic states depending on the temperature. High temperatures are on the right and low temperatures are on the left of the illustration. The gray-scale images to the left are representative PEEM-XMCD images obtained at 65 K. The length of the large and small mesospins are 1050 nm and 450 nm respectively. The width of the elements is the same, 150 nm.

As an example, the energy required for reversing the magnetization of the larger elements can be estimated to be larger compared to the smaller elements, solely from geometrical considerations. Thus, the large ele-

ments can be viewed as a source of quenched disorder, hindering the emergence of any medium- or long-range order within the lattice. While presenting a similar geometry, the modified-Shakti (mSH) consists of elements with the same activation energy and consequently mSH structures should not contain the same type of quenched disorder. Here we describe experiments addressing the influence of the two energy-scales on the obtained correlations and order in these Shakti lattices. We use the modified-Shakti lattice as a reference, allowing us to separate the contribution from the differences in the activation energies with respect to the Shakti lattice and those coming from missing mesospins as compared to square ASI. The experiments are performed with weakly interacting and thermally active elements, involving the transition from a paramagnetic state of the island material to a completely arrested collective order at lower temperatures.

As illustrated in Fig. 1, the material is paramagnetic at the highest temperature ($T \gg T_C$, far to the right) and the islands do not have any net magnetic moment. Below the intrinsic ordering temperature of the material (T_C), the elements become magnetic and a stray field is developed. This stray field is the source of the inter-island interactions, which also present a temperature dependence. There are two special cases which need to be considered: the strong and the weak coupling limit.

In the weak coupling limit the long-mesospins of a Shakti lattice will be arrested at temperatures below T_{B1} and their orientation will be uncorrelated. When the temperature is lowered below T_{B2} , the short-mesospins will also be arrested and the lattice as a whole "freezes". However, as the magnetic states of the long elements are random, an imprinted randomness should be imposed on the overall magnetic correlations of a Shakti lattice in the weak coupling limit.

In the strong coupling limit, the interplay between the two energy-scales will mask the difference between T_{B1} and T_{B2} and the magnetic states of the long-mesospins cannot be treated as independent of the shorter ones. Here, we focus on the weak coupling limit, associated to randomization of the obtained states of the long-mesospins. To verify the difference in the activation energy for the long and short elements in the SH lattice, we made two lattices consisting of non-interacting long- and short-mesospins and investigated the blocking temperature. Here we need to dwell on the experimental technique, to corroborate how the blocking temperatures were determined. The sampling time for every PEEM-XMCD image (t_s) defines the time window required for determining the magnetic state of a mesospin. At the lowest temperatures, all the magnetic states are frozen and the lattice can be imaged at arbitrary times, yielding the same result. However, if the magnetization reversal time of the mesospins is comparable or smaller than t_s , no magnetic contrast is obtained, which can be used

to determine the dynamics and also to determine the activation energy and thus blocking temperature of the elements. By imaging the structures at different temperatures, we could thereby determine if the elements flipped during the sampling time. Estimating the fraction of the identified mesospins as a function of temperature we were able to extract the activation energy for the elements. The ratio of the activation energy of the short- and the long-mesospins was determined to be 0.48(27) (for more details see Supplementary Materials).

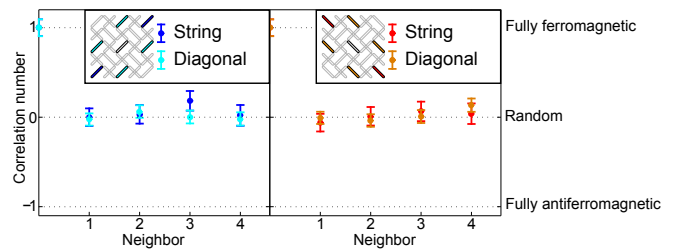


FIG. 2. **Long-mesospin correlations in the Shakti lattice.** The magnetic correlation for long-mesospins spatially oriented vertically/horizontally are shown in the left/right graph. In blue/red the correlation of long-mesospins which are oriented in a string and in light-blue/orange the correlation of the long-mesospins diagonally oriented are represented, as indicated in the inset. All correlations show that already the first neighbor is randomly oriented and therefore the magnetic orientations of the long-mesospins are not correlated.

The obtained correlation between the elements in a SH lattice is illustrated in Fig. 2. As seen in the figure, no correlation between the long-mesospins is observed. The results are therefore consistent with the simplified picture provided above, namely, a random arrangement of the long-mesospins arising from the weak interaction when crossing T_{B1} . At T_{B1} the short-mesospins are thermally active and under weak influence of the frozen long-mesospins. By the same token, the short-mesospin mediated interaction between the long-mesospins must be weak.

Having established the randomness of the magnetic states of the long-mesospins in a Shakti lattice, we can now address its implications on the overall order. To do this we need to define the possible states of the different types of vertices for both structures. The different vertex types are illustrated in Fig. 3a-c for both the SH and the mSH lattices. Both have vertices with coordination number three and four as illustrated in Fig. 3c. The subscript represents the number of mesospins forming a vertex, *e.g.* I_4 represents four elements forming a Type-I vertex. The mSH lattice has an additional degree of freedom as compared to the SH lattice, arising from the two-fold coordinated vertex having two possible states: Type- I_2 and Type- II_2 . The vertex statistics obtained from the three-fold and four-fold coordinated vertices are presented in Fig. 3d and 3e, respectively. Comparing the abundance

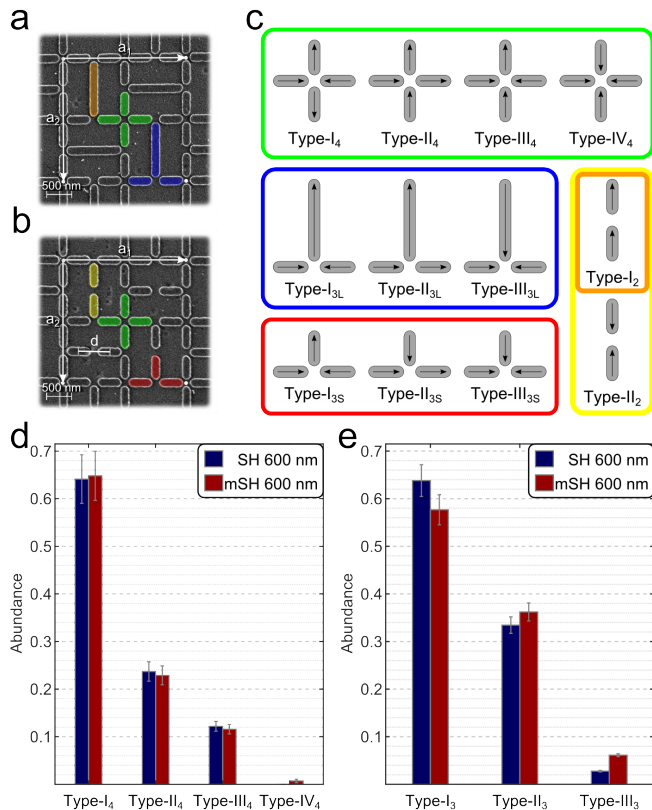


FIG. 3. **Vertex type definition and statistics for SH and mSH lattice.** SEM image of the SH (a) and mSH (b) lattice. The different vertex types are indicated by their respective colors. The real space base vectors for the Shakti lattice are defined along the x - and y -direction and each have a length of four times the lattice spacing ($d = 600$ nm). c, Definition of the vertex states for all different vertex types. While both lattices share the vertex type with a coordination number of four (green), the mSH lattice contains vertices with coordination number three (red) and two (yellow). The SH lattice consists also out of three-fold coordinated vertices (blue), but having a long-mesospin as perpendicular element. This long-mesospin can be described as a Type-I₂ vertex (orange) in comparison with the mSH two-fold coordinated vertex definition. The four- (d) and three-fold (e) coordinated vertex statistic for SH and mSH lattice show no significant differences.

of the different states with published data from Gilbert *et al.*¹⁷, we find that our results are consistent with the assumed weak coupling limit of the mesospins, in line with previous work on ASI structures^{3,4}. We conclude that there is no difference between the vertex states of the SH and mSH lattice, in line with previous findings¹⁷. These results unambiguously show that the obtained correlations are independent of the presence of the long islands, as judged from the population on the vertex level, for the three- and four-fold coordinated vertices. Investigating the two-fold coordinated vertices in the mSH lattice reveal that 34 % of the two-fold coordinated vertices are in their excited state, Type-II₂.

In order to elaborate more on the interplay between the two energy-scales, we have also extracted the abundance of various spin arrangements across the long-mesospins for the SH lattice and the two-fold coordinated vertices in the mSH lattice. The results are presented in Fig. 4 along with the estimated values for a random distribution, in the absence of any interaction between the mesospins under investigation. The low energy states (head to tail coupling) are more abundant than expected from a random distribution, for both SH and the mSH lattice.

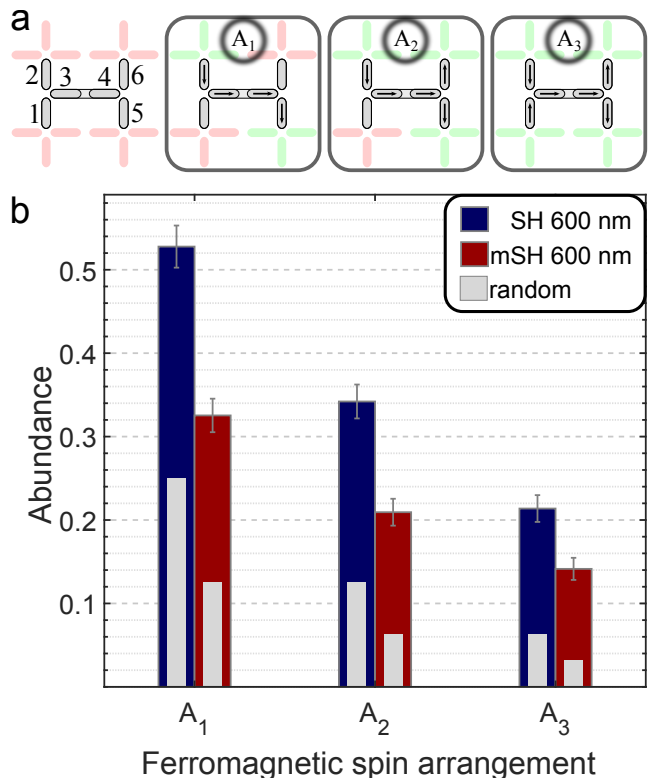


FIG. 4. **Spin arrangements across the long-mesospins / two-fold coordinated vertices.** a, Schematic representation of all mesospins linked to three-fold coordinated vertices (gray numbered islands). Presupposing a ferromagnetic alignment for mesospins 3 and 4, Type-I₂, we classify the arrangements of all other spins in three classes, denoted as A₁, A₂ and A₃. One representative spin arrangement for each of the three classes is depicted in a. The coupled four-fold coordinated vertices are indicated by the light-green islands. The number of coupled four-fold coordinated vertices across the Type-I₂ vertex for each class becomes then two for A₁, three for A₂ and all four for A₃. b, The abundance of these three classes is plotted for the SH (dark-blue) and the mSH (dark-red) lattice, revealing the distinct differences in the arrangement of the mesospins around the Type-I₂ vertex. A₁ and A₂ are averages of the four possible spin arrangements for these classes. The probability for each spin arrangement in a random mesospin state is represented with a gray inside bar for the SH and the mSH lattice.

Real space analysis tools have their limitations, as exemplified above. We therefore analyze the ordering

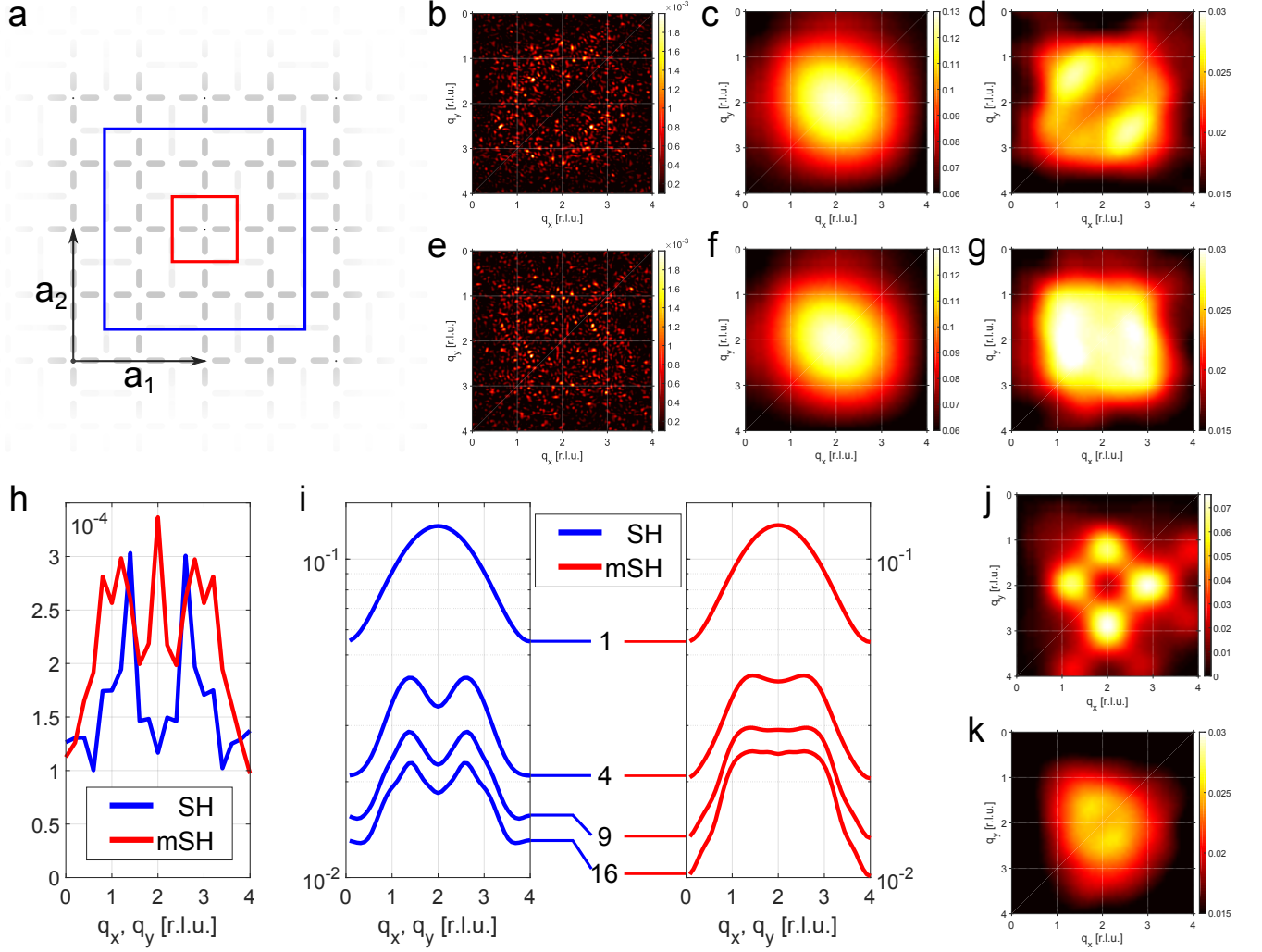


FIG. 5. **Spin structure factor as indicator for short-range order.** **a**, Illustration of the mesospin subset sizes used in the SSF calculations. The real space lattice vectors $\mathbf{a}_{1,2}$ which are used for the reciprocal lattice units (r.l.u.) are also shown. The real space input size for the averaged SSF for one (red – SSF **c/f**) and nine (blue – SSF **d/g**) vertices are highlighted. **b/e**, SSF maps of the whole four-fold vertex sub-lattice for the SH (**b**) and mSH (**e**) lattice are shown. **c-d/d-g**, The averaged SSF maps for SH (**c-d**) and mSH (**f-g**) lattice, with reduced real space input size. **h**, Diagonal line-profile for SSF map **b** (SH – blue) and SSF map **e** (mSH – red). **i**, Diagonal line-profile for the SSF of different input sizes for the SH (SSF **c-d**) and mSH (SSF **f-g**) lattice. Additionally to the SSF for one and nine vertices we also show the line-profile for the SSF of four and sixteen vertices. The modulation of the peak in the SSF maps at $(q_x, q_y) = (2, 2)$ [r.l.u.] is clearly distinguishable for the case of the SH lattice, strongly indicating a tiling for the two different configurations of Type I_4 vertices around the long-mesospins and the emergence of a short-range order (see also Supplementary Fig. 5). **j**, Averaged SSF of 10000 simulations of Type- I_4 tilings (input size 3×3 four-fold coordinated vertices) fulfilling the restrictions of the Shakti ground state manifold. **k**, Averaged SSF of 10000 simulations of four-fold coordinated vertex tilings (input size 3×3 four-fold coordinated vertices) following the vertex statistics from Fig. 3d.

within the lattice in Fourier space, by computing the so-called spin structure factor^{5–7} (SSF) given by:

$$I(\mathbf{q}) = \frac{1}{N^2} \sum_{(i,j=1)}^N \mathbf{s}_i^\perp \cdot \mathbf{s}_j^\perp \cdot e^{i\mathbf{q} \cdot (\mathbf{r}_i - \mathbf{r}_j)} \quad (1)$$

$I(\mathbf{q})$ is the intensity for a given scattering vector \mathbf{q} , N is the number of spins over which the SSF is calculated,

\mathbf{s}_i^\perp the spin component perpendicular to \mathbf{q} and \mathbf{r}_i is the position of the corresponding spin. Characteristic SSF maps for the SH and mSH lattice and for a certain \mathbf{q} -range as presented in Fig. 5b and 5e. A clear difference is observed when plotting diagonal line-profiles from these two maps, as shown in Fig. 5h.

The extended PEEM-XMCD images (see Supplementary Fig. 2), are just one out of many possible microstates. Reducing the size of the analysed microstates

by only looking at fraction of the sample reduces the lateral information, but increases the statistics when summing the results. Using a probe size of one four-fold coordinated vertex (see Fig. 5c and 5f) and summing over the whole sample, we get similar SSF maps for the SH and mSH lattices. This is expected as this input size resembles one four-fold coordinated vertex and therefore the resulting averaged SSF is a different representation of the vertex statistics shown in Fig. 3d. As these vertex statistics showed no significant differences, the SSF maps in Fig. 5c and Fig. 5f are similar as well, traceable also in the comparison of the top-most diagonal line-profiles in Fig. 5i. Expanding the SSF input to sixteen mesospins (four four-fold coordinated vertices) a clear difference between the SH and mSH appears (Fig. 5i). As already explained in the definition of the spin arrangements in Fig. 4, these SSFs represent an effective coupling among four four-fold coordinated vertices across a long-mesospin. Expanding the real space input to thirty-six mesospins (nine four-fold coordinated vertices) the differences in the SSF maps between the SH (Fig. 5d) and mSH (Fig. 5g) become even more pronounced (see also line profiles in Fig. 5i).

The hollow peak shape, as observed in the SSF of the SH lattice, is an indication for tiling valid for the Type- I_4 vertices around the long-mesospins. Coming back to the spin arrangements from Fig. 4, we identified the three different classes by the coupling of four-fold coordinated vertices via a Type- I_2 in the mSH lattice or a long-mesospin in the SH lattice. In the Shakti ground state manifold as described by Chern *et al.*¹⁶ the four-fold coordinated vertices are always in their lowest energy state, Type- I_4 (see definition Fig. 3c). These states have a two-fold degeneracy with states rotated by 90° in the plane, Type- $I_4(A)$ and Type- $I_4(B)$. Two Type- I_4 vertices which are coupled via the Type- I_2 or long-mesospin will be a Type- $I_4(A)$ and Type- $I_4(B)$. Therefore the distinct peak shape in the SSF can be explained by the enhanced coupling of Type- $I_4(A)$ to Type- $I_4(B)$ vertices via the long-mesospins in the SH lattice. The case of a random arrangement of the four-fold coordinated vertices (accordingly to the vertex state abundance in Fig. 3d) is presented in Fig. 5k and can be directly compared to the pattern resulting from a Type- I_4 tiling fulfilling the restrictions of the Shakti ground state manifold, shown in Fig. 5j. The representative maps from our experimental data are shown in Fig. 5d and g, for the SH and mSH lattice respectively. In the case of the SH lattice, the SSF map hints to a structure with a preference to a certain tiling of Type- I_4 vertices, which can also be traced to the amplitude of a dip in the peak, also seen in Fig. 5d and i. This effect is more pronounced than in the case of the mSH, as seen in in Fig. 5g and i, originating from the main difference between these two, being the presence of the long-mesospins.

Investigating systems containing multiple mesospin

sizes, we highlight the importance of the different length- and energy-scales on their magnetic ordering. As the thermalization of the short-mesospins in both systems is similar, no significant differences can be found for the abundance of different four-fold coordinated vertex types. However, investigations of the spatial arrangement of these vertices emphasize the influence of the long-mesospins. Looking at the results published by Gilbert *et al.*¹⁷ under this prism, could help explain some of their findings. In that case, the mSH has an almost perfect (100%) ground-state ordering on the four-fold coordinated vertex level, while the SH lattice has only about 80% of their four-fold coordinated vertices in the lowest energy state, Type- I_4 . These differences can be explained as results of the distinct length- and energy-scales. As the long-mesospins freeze-in into a pre-defined disordered sub-lattice the Shakti ground state manifold is restricted and shaped by the long-mesospin sub-lattice. Coupling of four Type- I_4 vertices via a long-mesospin, allows for 16 different Type- I_4 -tilings in total (see Supplementary Fig. 5). The Shakti ground state as defined by Chern *et al.*¹⁶ allows for 12 of these possible 16 tilings. The mSH lattice with its unique short-mesospin size can explore this complete manifold, but the SH lattice is restricted. The pre-defined disordered long-mesospin arrangement reduces effectively the possible states in the Shakti ground state manifold. The frozen long-mesospin restricts the Type- I_4 -tiling among four four-fold coordinated vertices to 7 out of 16 possible arrangements. As the systems grows in size, the Shakti ground state manifold gets even further reduced by each added frozen long-mesospin (for further information see Supplementary Materials).

In conclusion, we have used nano-patterned arrays with interacting magnetic mesospins, having distinct length- and energy-scales, in order to study the outcome on the magnetic order. The inclusion of the influence of multiple length- and energy-scales, on the magnetic ordering in such systems, is crucial for the explanation of the resulting magnetic structure. The hierarchy of these energy-scales, as well as the interplay between them, lie behind the complex emergent behavior and properties seen frequently across a range of natural systems¹⁸. The exploration of artificial spin systems resembling complicated physical processes in a ‘designer’ routine will potentially allow for a better understanding of problems in physics requiring multiple scale-analysis¹⁹.

Acknowledgments

The authors would like to thank C. Nisoli and G. W. Chern for valuable discussions. The authors acknowledge support from the Knut and Alice Wallenberg Foundation, the Swedish Research Council and the Swedish Foundation for International Cooperation in Research

and Higher Education. The patterning was performed at the Center for Functional Nanomaterials, Brookhaven National Laboratory, supported by the U.S. Department of Energy, Office of Basic Energy Sciences, under Contract No. DE-SC0012704. This research used resources of the Advanced Light Source, which is a DOE Office of Science User Facility under contract no. DE-AC02-05CH11231. This work is part of a project that has received funding from the European Union's Horizon 2020 research and innovation programme under grant agreement No 713171. U.B.A. acknowledges funding from the Icelandic Research Fund grants nr. 141518 and 152483.

Author contributions

H.S. D.G. and A.S. fabricated the samples. H.S., E.Ö., U.B.A., and V.K. performed the PEEM-XMCD experiments. H.S., E.Ö., I.A.C., D.G, T.P.A.H., B.H. and V.K. analyzed the data and contributed to theory development. H.S., B.H. and V.K. wrote the manuscript. All authors discussed the results and commented on the manuscript.

* henry.stopfel@physics.uu.se

- [1] M. J. Morrison, T. R. Nelson, and C. Nisoli, Unhappy vertices in artificial spin ice: new degeneracies from vertex frustration, *New Journal of Physics* **15**, 045009 (2013).
- [2] C. Nisoli, R. Moessner, and P. Schiffer, Colloquium: Artificial spin ice: Designing and imaging magnetic frustration, *Rev. Mod. Phys.* **85**, 1473–1490 (2013).
- [3] U. B. Arnalds, A. Farhan, R. V. Chopdekar, V. Kapaklis, A. Balan, E. T. Papaioannou, M. Ahlberg, F. Nolting, L. J. Heyderman, and B. Hjörvarsson, Thermalized ground state of artificial kagome spin ice building blocks, *Applied Physics Letters* **101**, 112404 (2012).
- [4] V. Kapaklis, U. B. Arnalds, A. Farhan, R. V. Chopdekar, A. Balan, A. Scholl, L. J. Heyderman, and B. Hjörvarsson, Thermal fluctuations in artificial spin ice, *Nature Nanotechnology* **9**, 514–519 (2014).
- [5] B. Canals, I.-A. Chioar, V.-D. Nguyen, M. Hehn, D. Lacour, F. Montaigne, A. Locatelli, T. O. Mentes, B. S. Burgos, and N. Rougemaille, Fragmentation of magnetism in artificial kagome dipolar spin ice, *Nature Communications* **7**, 11446 (2016).
- [6] Y. Perrin, B. Canals, and N. Rougemaille, Extensive degeneracy, Coulomb phase and magnetic monopoles in artificial square ice, *Nature* **540**, 410–413 (2016).
- [7] E. Östman, H. Stopfel, I.-A. Chioar, U. B. Arnalds, A. Stein, V. Kapaklis, and B. Hjörvarsson, The importance of the weak: Interaction modifiers in artificial spin ices, *arXiv* p. 1706.02127 (2017).
- [8] R. F. Wang, C. Nisoli, R. S. Freitas, J. Li, W. McConville, B. J. Cooley, M. S. Lund, N. Samarth, C. Leighton, V. H. Crespi, and P. Schiffer, Artificial spin ice in a geometrically frustrated lattice of nanoscale ferromagnetic islands, *Nature* **439**, 303–306 (2006).
- [9] E. H. Lieb, Exact Solution of the F Model of An Antiferroelectric, *Phys. Rev. Lett.* **18**, 1046–1048 (1967).
- [10] I. Syôzi, Statistics of Kagom Lattice, *Progress of Theoretical Physics* **6**, 306–308 (1951).
- [11] S. Zhang, I. Gilbert, C. Nisoli, G.-W. Chern, M. J. Erickson, L. O'Brien, C. Leighton, P. E. Lammert, V. H. Crespi, and P. Schiffer, Crystallites of magnetic charges in artificial spin ice, *Nature* **500**, 553–557 (2013).
- [12] J. P. Morgan, A. Stein, S. Langridge, and C. H. Marrows, Thermal ground-state ordering and elementary excitations in artificial magnetic square ice, *Nature Physics* **7**, 75–79 (2010).
- [13] A. Farhan, P. M. Derlet, A. Kleibert, A. Balan, R. V. Chopdekar, M. Wyss, L. Anghinolfi, F. Nolting, and L. J. Heyderman, Exploring hyper-cubic energy landscapes in thermally active finite artificial spin-ice systems, *Nature Physics* **9**, 375–382 (2013).
- [14] A. Farhan, P. M. Derlet, A. Kleibert, A. Balan, R. V. Chopdekar, M. Wyss, J. Perron, A. Scholl, F. Nolting, and L. J. Heyderman, Direct Observation of Thermal Relaxation in Artificial Spin Ice, *Physical Review Letters* **111**, 057204 (2013).
- [15] V. Kapaklis, U. B. Arnalds, A. Harman-Clarke, E. T. Papaioannou, M. Karimipour, P. Korelis, A. Taroni, P. C. W. Holdsworth, S. T. Bramwell, and B. Hjörvarsson, Melting artificial spin ice, *New Journal of Physics* **14**, 035009 (2012).
- [16] G.-W. Chern, M. J. Morrison, and C. Nisoli, Degeneracy and Criticality from Emergent Frustration in Artificial Spin Ice, *Physical Review Letters* **111**, 177201 (2013).
- [17] I. Gilbert, G.-W. Chern, S. Zhang, L. O'Brien, B. Fore, C. Nisoli, and P. Schiffer, Emergent ice rule and magnetic charge screening from vertex frustration in artificial spin ice, *Nature Physics* **10**, 670–675 (2014).
- [18] P. W. Anderson, More Is Different, *Science* **177**, 393–396 (1972).
- [19] K. G. Wilson, Problems in Physics with many Scales of Length, *Scientific American* **241**, 158–179 (1979).
- [20] M. Pärnaste, M. Marcellini, E. Holmström, N. Bock, J. Fransson, O. Eriksson, and B. Hjörvarsson, Dimensionality crossover in the induced magnetization of Pd layers, *Journal of Physics: Condensed Matter* **19**, 246213 (2007).

METHODS

Sample fabrication

The magnetic nano-arrays were produced by a post-growth patterning process, applied on a thin film of δ -doped Palladium (Iron) as described in reference²⁰. A thick bottom layer of Pd (40 nm) is followed by the 2.0 mono layers of Fe, defining the Curie-temperature, $T_C = 400$ K²⁰, as well as the thermally active temperature range for the δ -doped Pd(Fe). The post-patterning was carried out at the Center for Functional Nanomaterials (CFN), Brookhaven National Laboratory in Upton, New York. A positive high resolution e-Beam resist

(ZEP520A) was employed to create a Chromium mask of the nano-structures with e-Beam lithography. The magnetic structures were formed by Argon milling. All investigated structures are produced on the same substrate from the same layer, ensuring identical material properties as well as the same thermal history for all the investigated structures. Each array had a spatial dimension of $200 \times 200 \mu\text{m}^2$.

PEEM-XMCD

The magnetic state of the patterns were determined using Photoemission-Electron-Microscopy (PEEM) employing the X-ray Magnetic Circular Dichroism (XMCD) at the L_3 -edge of Fe (707.2 eV)⁴. The experimental studies were performed at the 11.0.1 PEEM3 beamline at the Advanced Light Source, in Berkley, California. The islands were oriented 45° with respect to the incoming X-ray beam, to enable identification of the magnetization direction of the mesospins. Multiple, partially overlapping, PEEM-XMCD images were acquired and stitched together to one large image containing over 4000 mesospins for each of the investigated lattices. The images used for determining the magnetic states were taken at 65 K, far below the Curie-temperature and the blocking temperatures, of the short- and long-mesospins.

Spin Structure Factor of subsets

Since the SH and the mSH lattice have different lattice points, \mathbf{r}_i , for the long- and two short-mesospins, the differences in the SSF of the SH and mSH data is dominated by this structural differences. Therefore we calculate the SSF accordingly to equation (1), in the same manner as more detailed explained in Östman *et al.*⁷, but only using the mesospins of the vertices with a coordination number of four. Since this subset of mesospins is the same in the SH and mSH lattice, differences in the SSF represent different ordering among these subset of spins. While SSF maps Fig. 5b and 5e are calculated throughout the whole data, Fig. 5c-d and 5f-g are averaged SSF of certain real space sizes, indicated in Fig. 5a. Calculating the SSF for one vertex, only 4 mesospins, and executing this for all vertices in the measured array, we get the SSF Fig.

5c and 5f representing the vertex counts for the vertices with coordination number four. The SSF for four or nine vertices, 16 or 36 mesospins, are the indicator for higher short-range order in the SH lattice. The line-profiles in Fig. 5h-i are diagonal cuts through the respective SSF-maps. For Fig. 5h nine lines needed to be averaged and fifteen points are binned into one to reduce the speckle information of the data, for Fig. 5i binning was not necessary since the averaging of multiple SSF already eliminate these speckle information. The SSF maps in Fig. 5j-k are averaged from 10000 random arrangements of nine vertices. Fig. 5j represent a Type-I₄ tiling fulfilling the criteria for the Shakti ground state manifold. This SSF map shows the hollow peak similar to the SSF maps of the SH lattice (Fig. 5d). Fig. 5k shows the average of 10000 SSF maps of nine vertices, where the vertices are randomly chosen out of the vertex statistics from Fig. 3d.

Spin arrangements

In Fig. 4 the orientation of the mesospins in respect to the long-mesospin (SH) or the two-fold coordinated vertex (mSH) are investigated. In the three vertex coupling classes A_1 , A_2 and A_3 a total of nine different ferromagnetic spin arrangements are investigated. A detailed analysis of all nine spin arrangements can be found in the supplementary material. In Fig. 4b A_1 and A_2 are averages of four different spin arrangements (C_1 - C_4 and C_5 - C_8 , see supplementary materials Fig. 4), which have the same characteristic. In the case of A_1 , one mesospin (mesospin 1 or 2 in schematic 4a) is ferromagnetic aligned to the long-mesospin (or the two ferromagnetic aligned mesospins of the two-fold coordinated vertex) and one mesospin on the other side (mesospin 5 or 6 in Fig. 4a). For A_2 one mesospin on one side is ferromagnetic aligned with two mesospins on the other side of the long-mesospin (or the two ferromagnetic aligned mesospins of the two-fold coordinated vertex). A_3 represents the lowest energy configuration for these five (six in the mSH) mesospins and arranges all mesospins (mesospin 1, 2, 5 and 6 in schematic Fig. 4a) ferromagnetically with respect to the long-mesospin (or the two ferromagnetic aligned mesospins of the two-fold coordinated vertex).

Magnetic order and energy-scale hierarchy in artificial spin ice

Henry Stopfel,^{1,*} Erik Östman,¹ Ioan-Augustin Chioar,¹ Unnar Arnalds,² David Greving,³

Thomas P. A. Hase,³ Aaron Stein,⁴ Björgvin Hjörvarsson,¹ and Vassilios Kapaklis¹

¹*Department of Physics and Astronomy,*

Uppsala University, Box 516, SE-75120, Uppsala, Sweden

²*Science Institute, University of Iceland, Reykjavik, Iceland*

³*Department of Physics, University of Warwick, Coventry, United Kingdom*

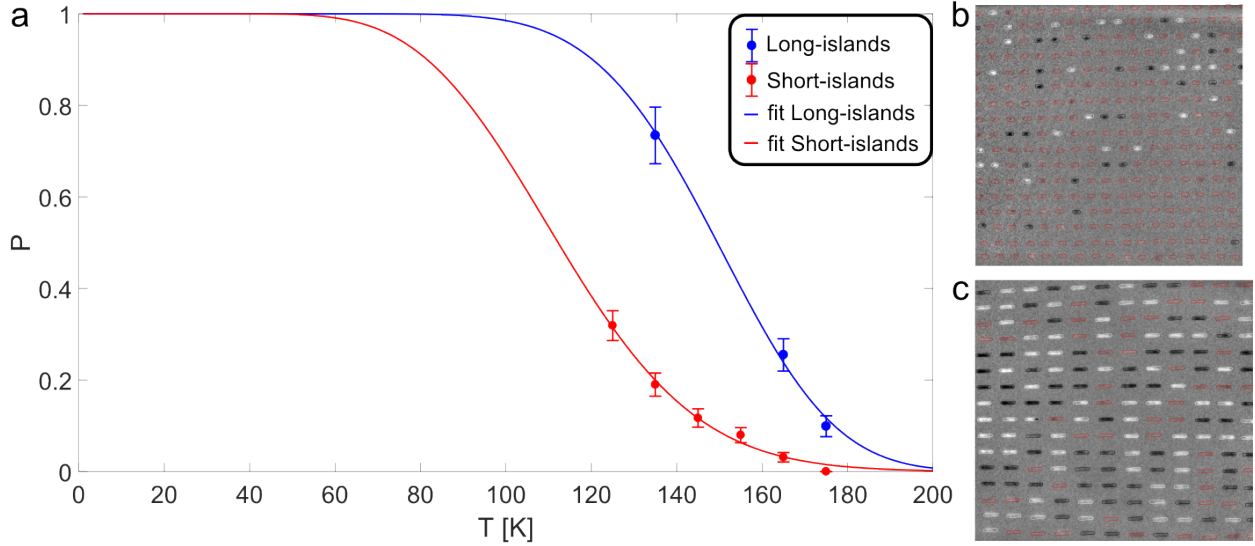
⁴*Center for Functional Nanomaterials,*

Brookhaven National Laboratory, Upton, New York 11973, USA

(Dated: December 14, 2024)

arXiv:1711.07754v1 [cond-mat.mtrl-sci] 21 Nov 2017

ACTIVATION ENERGY



Supplementary Figure 1. **Temperature dependent measurements of thermal activities of uncoupled mesospins.** **a**, Fractions of identifiable magnetic islands during a PEEM-XMCD measurement of 300 s and their corresponding fits. Both island types have a width of 150 nm, while the short-islands have a length of 450 nm and the long of 1110 nm. An exemplary PEEM-XMCD image for the short- (**b**) and long-islands (**c**) is presented for the measurement at 135 K.

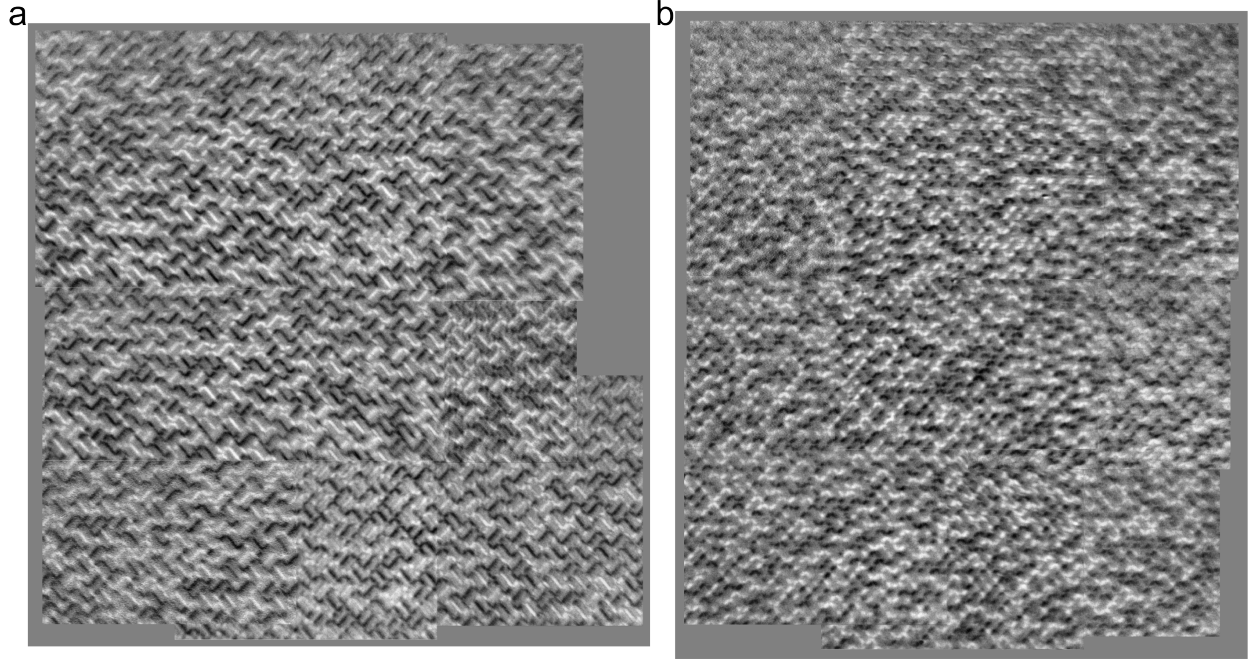
The fractions of identifiable islands for short- (red) and long-islands (blue) can be fitted with the following function:

$$P(T) = \exp\left(-\frac{A}{\exp\left(\frac{B}{T}\right)}\right) \quad (1)$$

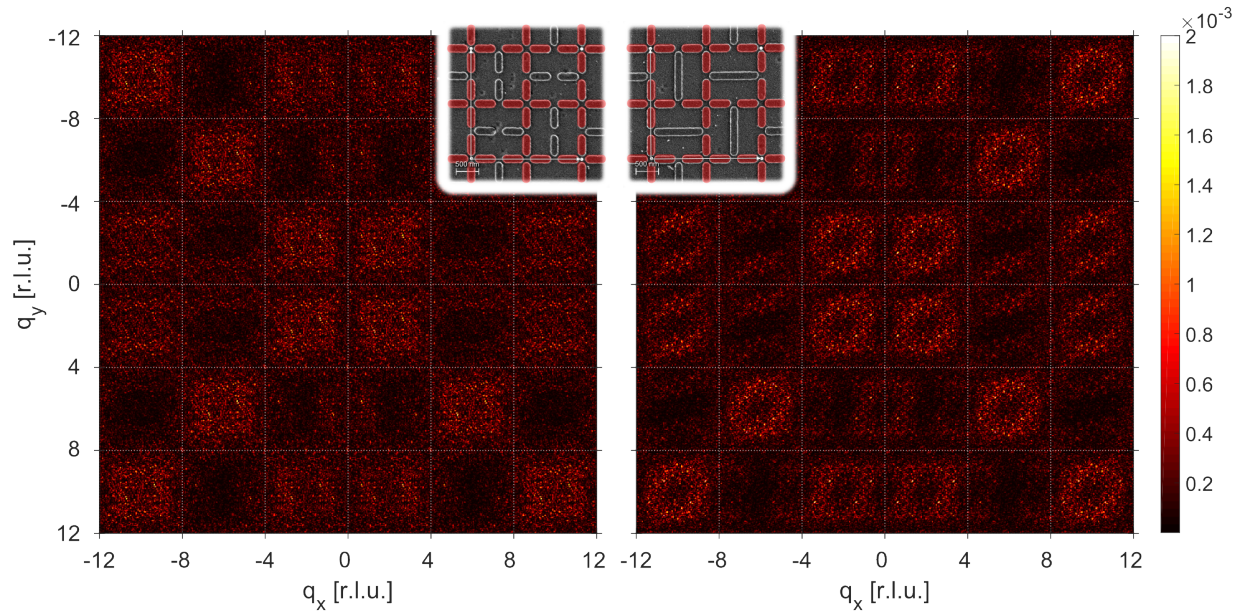
$$A = \frac{t_s}{\tau_0} = \frac{300 \text{ s}}{\tau_0} \quad (2)$$

$$B = \frac{E}{k_B} \quad (3)$$

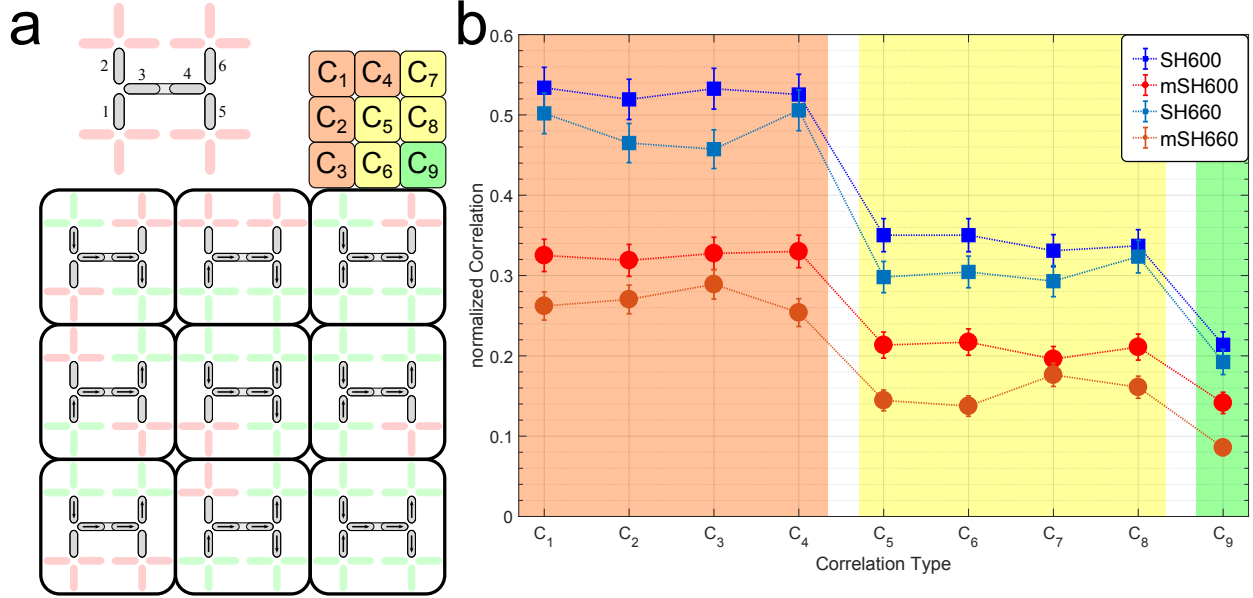
Equation (1) represents the probability of a magnetic element not having altered its magnetization direction after a time period t_s .[?] Where T is the temperature and A and B are the fitting parameters, and with $t_s = 300$ s in equation (2) being the measurement time for the PEEM-XMCD image. The τ_0 in equation (2) is the inverse attempt frequency^{1?}, which has been fitted here. In equation (3) is E the activation energy and k_B Boltzmann's constant, yielding fitting parameter B in Kelvin. The ratio of the activation energy for short- ($B_{short} = 562$ K) and long-islands ($B_{long} = 1159$ K) can be determined from the fits to Suppl. Fig. 1a and is to be 0.48(27).



Supplementary Figure 2. **PEEM-XMCD measurements of the Shakti lattices.** Stitched PEEM-XMCD images of the SH (a) and mSH (b) lattices with a lattice parameter of 600 nm.



Supplementary Figure 3. **Spin structure factor over extended q-space for four-fold coordinated vertex sub-lattice of the SH (right) and mSH (left).** The real space lattice vectors as well as the sub-lattice of four-fold coordinated vertices are as indicated in the insets.

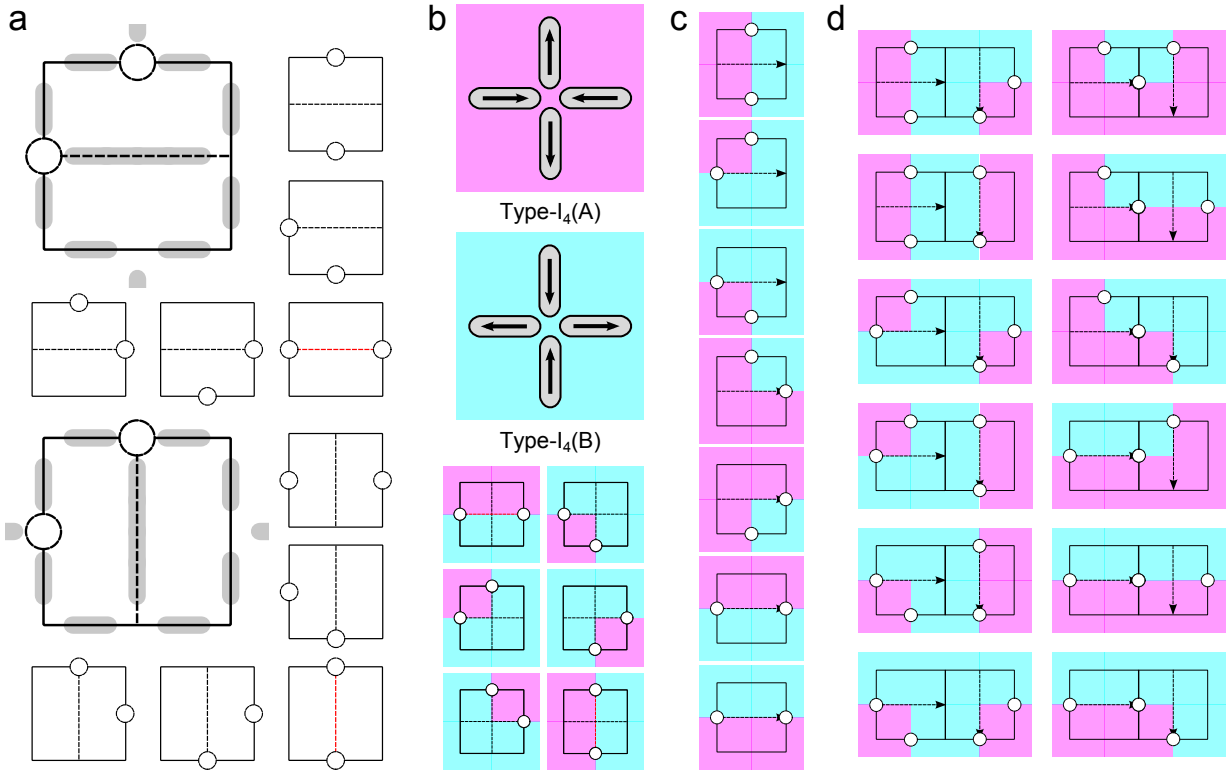


Supplementary Figure 4. **Spin arrangement around the long-mesospin (Type-I₂).** **a**, Illustration of the five (six in mSH) islands which are considered in the spin arrangements. Adjacent islands are indicated by light red and in the different representation of the spin arrangements C₁-C₉ with light green if correlated over the long-mesospin (Type-I₂). All different spin arrangements are illustrated in **a** as well. **b**, Abundance of the different spin arrangements, for the SH (blue – squares) and mSH (red – circles) lattices. The data are shown for 600 and 660 nm lattice parameters.

SPIN ARRANGEMENTS

All nine possible spin arrangements C₁–C₉, for the short- and long-mesospins (depending on the lattice) around the three-fold coordinated vertices are depicted in Fig. 4a. In order to simplify the analysis, we restrict ourselves to a ferromagnetic arrangement of the mesospins for the two-fold coordinated vertices. The abundance of the spin arrangements is presented in Fig. 4b. These spin arrangements can be categorized into three groups marked with orange, yellow and green. Group one (orange – A₁), are arrangements C₁ – C₄ connecting one mesospin, and the respective vertex, with another mesospin on the other side of the long-mesospin (two short-mesospins). The second group (yellow – A₂), are arrangements C₅ – C₈ in which one mesospin on one side is in ferromagnetic alignment with the long-mesospin (two short-mesospins) and two mesospins on the other side. Finally, the last arrangement, C₉, is a lowest energy state for this subset of mesospins.

Roughly 53% of all investigated long-mesospin connections of the SH have at least two vertices being correlated to each other ($C_1 - C_4$), but only 32% of them are correlated in the mSH via the two short-islands. Similar differences in the correlations can also be found for the other spin arrangements ($C_5 - C_9$). One indication for these behaviors is the high abundance (over 30%) of Type-II₂ excitations in vertices with coordination number two, which are therefore unable to mimic the SH order.



Supplementary Figure 5. **Shakti ground state manifold in plaquettes.** **a**, Illustration of the Shakti ground state manifold in a plaquette as introduced by Chern *et al.*². In the Shakti ground state all four-fold coordinated vertices are in their lowest energy state, Type-I₄, and 50% of the three-fold coordinated vertices are in their lowest energy state, Type-I₃, and 50% are in the excited state, Type-II₃. These excitations are represented with a circle in the plaquette illustration by Chern *et al.* **b**, Equivalent representation of the Shakti ground state manifold for a plaquette, focusing on the Type-I₄ tiling at the four-fold coordinated vertices. All Type-I₄ tilings for a predefined long-mesospin direction are illustrated for one **(c)** and two plaquettes **(d)**.

TYPE-I₄-TILING

The ground state manifold of the Shakti lattice was described by Chern *et al.*² and is best to explain on the size of a plaquette. In Fig. 5a is the extend of a plaquette illustrated and the representation of the Shakti ground state manifold of such a plaquette shown. Lines illustrate lowest energy states, but the circles at the three-fold coordinated vertices mark the position of Type-II₃ excitations. In the Shakti ground state a plaquette inhabits two of such excitations, at any of their four three-fold coordinated vertices. As all the four-fold coordinated vertices are in their lowest energy state, Type-I₄, we represent the tiling of the two degenerated Type-I₄ vertices on the bases of a plaquette in Fig. 5b.

The excitations in the Shakti lattice are located at the boundaries between Type-I₄(A) and Type-I₄(B) vertices. We discussed in the main text, that the pre-defined long-mesospins in the SH lattice will restrict the possible Type-I₄-tilings. This effect is illustrated in Fig. 5c-d for one and two plaquettes. All 7 (out of 16) Type-I₄-tilings accessible, by simultaneously remaining in the Shakti ground state manifold, regarding the given long-mesospin direction are illustrated in Fig. 5c. For two pre-defined long-mesospins (two neighboring plaquettes – Fig. 5d) just 13 (out of 64) Type-I₄-tilings remain in the Shakti ground state manifold.

* henry.stopfel@physics.uu.se

- [1] V. Kapaklis, U. B. Arnalds, A. Farhan, R. V. Chopdekar, A. Balan, A. Scholl, L. J. Heyderman, and B. Hjörvarsson, Thermal fluctuations in artificial spin ice, *Nature Nanotechnology* **9**, 514–519 (2014).
- [2] G.-W. Chern, M. J. Morrison, and C. Nisoli, Degeneracy and Criticality from Emergent Frustration in Artificial Spin Ice, *Physical Review Letters* **111**, 177201 (2013).